Highly Selective O_2 Reduction to H_2O_2 Catalyzed by Cobalt Nanoparticles Supported on Nitrogen Doped Carbon in Alkaline Solution

*Jun Wu[a], Asad Mehmood[a], Guohui Zhang[a], Shuang Wu[b], Ghulam Ali[c], Anthony Kucernak[a]**

[a]Department of Chemistry, Imperial College London, South Kensington Campus, London SW7 2AZ, United Kingdom

[b]SINOPEC Shanghai Research Institute of Petrochemical Technology, Shanghai 201208, People's Republic of China

[c]US-Pakistan Center for Advanced Studies in Energy (USPCASE), National University of Science and Technology (NUST), H-12, Islamabad, 44000, Pakistan

1. Abstract

We report the synthesis of cobalt nanoparticles supported on nitrogen-doped carbon (Co_{NPs}@N/C) which can reduce O_2 into H_2O_2 with high selectivity (up to 93%) in 0.1M KOH electrolyte and retain high activity even after 10 hour polarization (>90%). The catalyst achieves a current density of 1 mA cm^{-2} at 0.76 V(RHE) and achieves a peroxide production rate of ~3.8mol_{H2O2} g_{Co}^{-1} h^{-1} over a ten-hour period. Our study also highlights the requirement for good peroxide production catalysts to be poor hydrogen peroxide disproportionation catalysts. We show how the high activity of the Co_{NPs}@N/C catalyst is correlated with low activity towards the peroxide disproportionation reaction.

Key words: Electrocatalysis, Oxygen Reduction Reaction, H_2O_2 Production, Heteroatom doping, Carbon

2. Introduction

Hydrogen peroxide (H_2O_2) is an important, environmentally friendly oxidant utilized widely in various chemical processes including wastewater treatment, paper industry and green chemical synthesis.[1-4] Currently, H_2O_2 is industrially manufactured by the anthraquinone oxidation process. The anthraquinone

technology requires direct use of hydrogen and oxygen gases and involves sequential hydrogenation, oxidation of anthraquinone molecules and extraction of H_2O_2.[5-6] This multiple-step procedure generates a large quantity of waste chemicals along with many safety issues including the storage and transportation of concentrated H_2O_2.[7] Instead, the direct electrosynthesis of H_2O_2 through oxygen reduction reaction (ORR) via a two-electron step ($O_2 + 2H^+ + 2e^- \rightarrow H_2O_2$ under acidic conditions, or $O_2 + H_2O + 2e^- \rightarrow HO_2^- + OH^-$ under basic conditions) under room temperature has attracted significant attention.[8-12] With oxygen reduction and water oxidation occurring at the cathode and anode under an external voltage bias, respectively, the only byproduct is hydroxyl, indicative of the environmental friendliness of such atom economic method.[6, 13] Even with the advantages of the direct electrosynthesis H_2O_2, the oxygen reduction is kinetically sluggish and influenced by the competitive four-electron pathway to reduce O_2 to undesired water, which will notably reduce the H_2O_2 yield. Thus, suitable electrocatalysts with high reactivity for ORR and selectivity towards H_2O_2 are sought after. Nowadays, the state-of-the-art catalysts for the electrosynthesis of H_2O_2 are largely based on noble metals (e.g. Au and Pd) and their alloy (e.g. Pt-Hg, Ag-Hg, and Pd-Hg).[14-17] Those noble metal electrocatalysts drive the ORR via a two-electron pathway with small overpotential as well as high H_2O_2 selectivity. However, the scarcity and high cost of those noble metals, as well as the high toxicity of Hg, limit their large-scale applications. Therefore, the development of an alternative efficient electrocatalyst for the electrosynthesis of H_2O_2 has attracted wide attention and showed a great potential to substituting the noble metal catalysts.[10, 18-20] Despite the resuscitating research interest in this field, one major challenge is to design an appropriate catalyst that can convert O_2 into H_2O_2 efficiently over a wide potential range to allow high throughput H_2O_2 production. Here we report the synthesis of cobalt nanoparticles supported on nitrogen-doped carbon (denoted as Co_{NPs}@N/C) which can catalyze the ORR via a $2e^-$ reduction selectively to H_2O_2 over a wide potential range in alkaline solution. This catalyst is compared to atomically dispersed cobalt single atom motifs coordinated in nitrogen and carbon matrix catalysts (denoted as Co-N_x/C) and the metal-free

nitrogen doped carbon (denoted as N/C). A comparison is also given with cobalt nanoparticles deposited on XC-72R carbon (Co_{NPs}@C). We compare H_2O_2 electrosynthesis performance across all four catalysts. The approach shown in this work demonstrates that it is possible to choose a nitrogen-containing carbon precursor with suitable morphology to prepare versatile, scalable and highly active carbon-based electrocatalysts for the selective production of H_2O_2 from oxygen via a $2e^-$ reduction.[21] We show that the best catalyst also has the lowest rate of activity towards the hydrogen peroxide disproportionation reaction, an extra important requirement for hydrogen peroxide formation.

Experiments and Methods

3.1 Synthesis of Co-N-C catalyst

Metal-free N/C:[21] 0.5 g 1,5-diaminonaphthalene (97%, Sigma Aldrich) and 0.5 g $(NH_4)_2S_2O_8$ (98%, Sigma Aldrich) were firstly dispersed in 50 mL ethanol (absolute, VWR). The mixture was then stirred for 24 h at 25 °C to obtain 1,5-diaminonaphtalene oligomers. Then the obtained dispersion was heated to 80 °C to evaporate ethanol and drive the oligomers polymerization. The as-synthesized grey powder was then loaded in a high alumina combustion boat and heated in the tube furnace to 1000 °C at a heating rate of 10 °C min^{-1} and held for 2 h under N_2 (BOC N6.0 grade). The remaining black powder was further refluxed under 120 °C for 8 h in 0.5 M H_2SO_4 to remove possible metal impurities and then filtered with a polycarbonate (PCTE) membrane filter (0.2 Micron, 47mm, Sterlitech). After filtering and drying at 60 °C overnight, the **N/C** catalyst was ready to use.

Co-N_x/C: 1 g 1,5-diaminonaphthalene (97%, Sigma Aldrich) was firstly dissolved in 220 mL ethanol (absolute, VWR). Then 40 mg $CoCl_2 \cdot 6\ H_2O$ (98 %, Sigma-Aldrich) was dissolved in 20 mL ethanol (absolute, VWR) and added. 1g $(NH_4)_2S_2O_8$ (98 %, Sigma-Aldrich) was then dissolved in 10 mL H_2O (MilliQ 18.2 MΩ cm) and also added to the above solution after 10 minutes. The mixture was stirred at 25 °C for 22 h and then the ethanol was evaporated under 80 °C and the remaining black powder was loaded

in an high alumina combustion boat and then subjected to pyrolysis in tube furnace to 950 °C at a heating rate of 10 °C min^{-1} and held for 2 h under N_2 (BOC N6.0 grade). The remaining black powder was refluxed under 120 °C for 8 h in 0.5 M H_2SO_4 and then filtered with a polycarbonate (PCTE) membrane filter (0.2 Micron, 47mm, Sterlitech). After filtering and drying at 60 °C overnight, the **Co-N_x/C** catalyst was ready to use.

Co_{NPs}@N/C: 350 mg 1,5-diaminonaphtalene (97%, Sigma Aldrich) and 214 mg $CoCl_2 \cdot 6\ H_2O$ (98%, Sigma-Aldrich) were firstly dispersed in 50 mL ethanol (absolute, VWR). The mixture was stirred for 24 h at 25 °C to obtain 1,5-diaminonaphtalene oligomers. Then the dispersion was heated to 80 °C to evaporate ethanol and drive the oligomers polymerization. The remaining dark powder was then loaded in an high alumina combustion boat and heated in the tube furnace to 1000 °C at a heating rate of 10 °C min^{-1} and held there for 2 h under N_2 (BOC N6.0 grade). The resulting black powder was refluxed under 120 °C for 8 h in 0.5 M H_2SO_4 and then filtered with a polycarbonate (PCTE) membrane filter (0.2 Micron, 47mm, Sterlitech). After being filtered and dried at 60 °C overnight, the **Co_{NPs}@N/C** catalyst was ready to use. It is worth noting that no additional oxidant (i.e., $(NH_4)_2S_2O_8$) was added in this synthesis, the autoxidation of the excessive $CoCl_2$ to the metal +3 species by O_2 in the solution was found to facilitate the oxidative polymerization.[21-22]

Co_{NPs}/C: 350 mg Carbon black powder (350mg, Vulcan XC72R, Cabot) and 214 mg $CoCl_2 \cdot 6\ H_2O$ (98%, Sigma-Aldrich) were dispersed in 50 mL ethanol (absolute, VWR). The mixture was stirred for 24 h at 25 °C to obtain the well dispersed precursor. The dispersion was then heated to 80°C to evaporate ethanol and pyrolyzed in a tube furnace to 1000 °C at a heating rate of 10 °C min^{-1} and held for 2 h under N_2 (BOC N6.0 grade). The remaining black powder was refluxed under 25 °C for 8 h in 0.5 M H_2SO_4 and then filtered with a polycarbonate (PCTE) membrane filter (0.2 Micron, 47mm, Sterlitech). After being filtered and dried at 60 °C overnight, the **Co_{NPs}/C** catalyst was ready to use.

3.2 Catalysts characterization

X-ray diffraction (XRD) was performed on a Bruker AXS D2 Phaser Desktop X-ray Diffractometer. X-ray photoelectron spectroscopy (XPS) was obtained on a Thermo Scientific K-Alpha X-ray Photoelectron Spectrometer system (Al K α, 1486.6 eV). Transmission electron microscope (TEM) analysis was obtained from a FEI Titan Krios^{TM} G3. Inductively coupled plasma atomic emission spectrometry (ICP-AES) was carried out on an IRIS Intrepid II XSP (Thermo Electron Corporation, USA). Raman spectra were recorded on an inVia^{TM} confocal Raman microscope. N_2 adsorption was performed on an Autosorb iQ (Quantachrome Instruments) to obtain the Brunauer-Emmett-Teller (BET) surface area. X-Ray Fluorescence analysis (XRF) was performed on a Bruker S2 PICOFOX. The coordination environment of Co atoms in the synthesized catalysts was examined by X-ray absorption spectroscopy (XAS). The XAS spectra were recorded in the fluorescence mode at 10C beamline of Pohang Accelerator Laboratory (PAL). As reference materials, spectra of Co(II) phthalocyanine ($Co^{II}Pc$) and metallic cobalt foil were also measured. X-ray absorption near edge structure (XANES) and Fourier transformation (FT) of the extended X-ray absorption fine structure (EXAFS) spectra were processed in the k-range of 3 - 11 $Å^{-1}$ using Athena software.[23]

3.3 Electrochemical experiments

The electrochemical experiments were performed using a rotating ring disk electrode (RRDE) (Pine Instruments, model AFE6R1AU with glassy carbon as disk with a concentric gold ring and rotator model AFMSRCE). The inks consisted of a known amount of catalyst in IPA (VWR) and H_2O (MilliQ 18.2 MΩ cm) mixture solution (volume ratio = 1:1). Besides, Nafion solution (5 wt%, Sigma-Aldrich) following a weight ratio of 0.034 of Nafion to catalyst was also added.[24] The inks were drop casted on the glassy carbon disk and dried to make a final catalysts loading of 0.1 mg cm^{-2}. A three-electrode glass cell was used. A

reversible hydrogen electrode and a glassy carbon rod were used as the reference electrode and the counter electrode, respectively. The RHE reference electrode was ionically connected to the main part of the electrochemical cell via a *Luggin-Haber*-Capillary. A potentiostat (Autolab, model PGSTAT302N) was used during all the electrochemical measurements in this work to control potential or current. Steady state ORR polarization curves with iR compensation were obtained under 30 mV step potentials with 30s hold in O_2-saturated 0.1 M KOH (VWR Chemicals, 85.3%). Ultrapure N_2 and O_2 (BIP plus-X47S, Air products) were used to purge the 0.1 M KOH electrolytes. Cleaning protocol was performed before every electrochemical experiment to obtain stable baselines. The cleaning protocol consisted of 20 cycles at 100 mV s^{-1}, 10 cycles at 10 mV s^{-1} and 5 cycles at 5 mV s^{-1} in N_2-saturated 0.1 M KOH, sequentially, in the potential window of 1.05 - -0.2V *vs* RHE. Selective poisoning of the electrocatalysts was investigated by collecting the RRDE ORR polarization curves in O_2-saturated 0.1 M KOH before and after dosing the KCN solution into the electrolyte to obtain a total CN^- concentration of 10 mM. In order to avoid any changes related to the catalyst loading, the same batch of the catalyst-coated glassy carbon electrode was used for the whole set of experiments.[25] In contrast to many other papers in this area which detect hydrogen peroxide on Pt ring electrodes, at 1.2-1.3 V, we used a gold ring at a potential of 1.5 V. The reason for this is twofold – (a) as gold is much less active for oxygen evolution, it can be used for H_2O_2 oxidation at higher potential (b) it provides a more stable response for the H_2O_2 oxidation. The peroxide oxidation current was corrected by subtracting the ring current obtained under nitrogen from the ring current under oxygen. The percentage of peroxide produced during the ORR was calculated using the following equation:

$$H_2O_2(\%) = \frac{2I_r/N}{I_d + I_r/N} \times 100 \quad (1)$$

where N is the collection efficiency of the RRDE, and I_d and I_r are the measured disk and ring currents, respectively. The electron transfer number during the ORR process at the disk electrode was calculated as follows:

$$n = \frac{4I_d}{I_d + I_r/N} \quad (2)$$

Moles of H_2O_2 produced during the ORR was calculated as follows:

$$H_2O_2\ (mol\ s^{-1}) = \frac{I_r/N}{2F} \quad (3)$$

where F is the Faraday constant. Quantification of hydrogen peroxide produced during a 10-hour polarization was performed using a colorimetric method involving the reaction of product H_2O_2 with TiO^{2+} (details in SI, Figure S11 and associated text).

3.4 Hydrogen peroxide determination

A hydrogen peroxide colorimetric assay involving reacting aliquots of H_2O_2 containing electrolyte with 0.1 M $TiOSO_4$ solution was used to determine the concentration of H_2O_2 in solution. Assessment of the concentration involved measuring the absorbance at 407 and nm using a molar absorbance of 3.86 M^{-1} cm^{-1} (see supplementary section 9 for discussion and calibration graph).

Hydrogen peroxide decomposition was determined by preparing 100 ml of solution containing 0.1 M KOH, 0.5 mM H_2O_2 (similar to the concentration produced during long term electrolysis), and 1 mg dm^{-3} catalyst. The reaction mixture was stirred, and aliquots were removed at predetermined periods, filtered, and the amount of hydrogen peroxide determined through the above colorimetric assay.

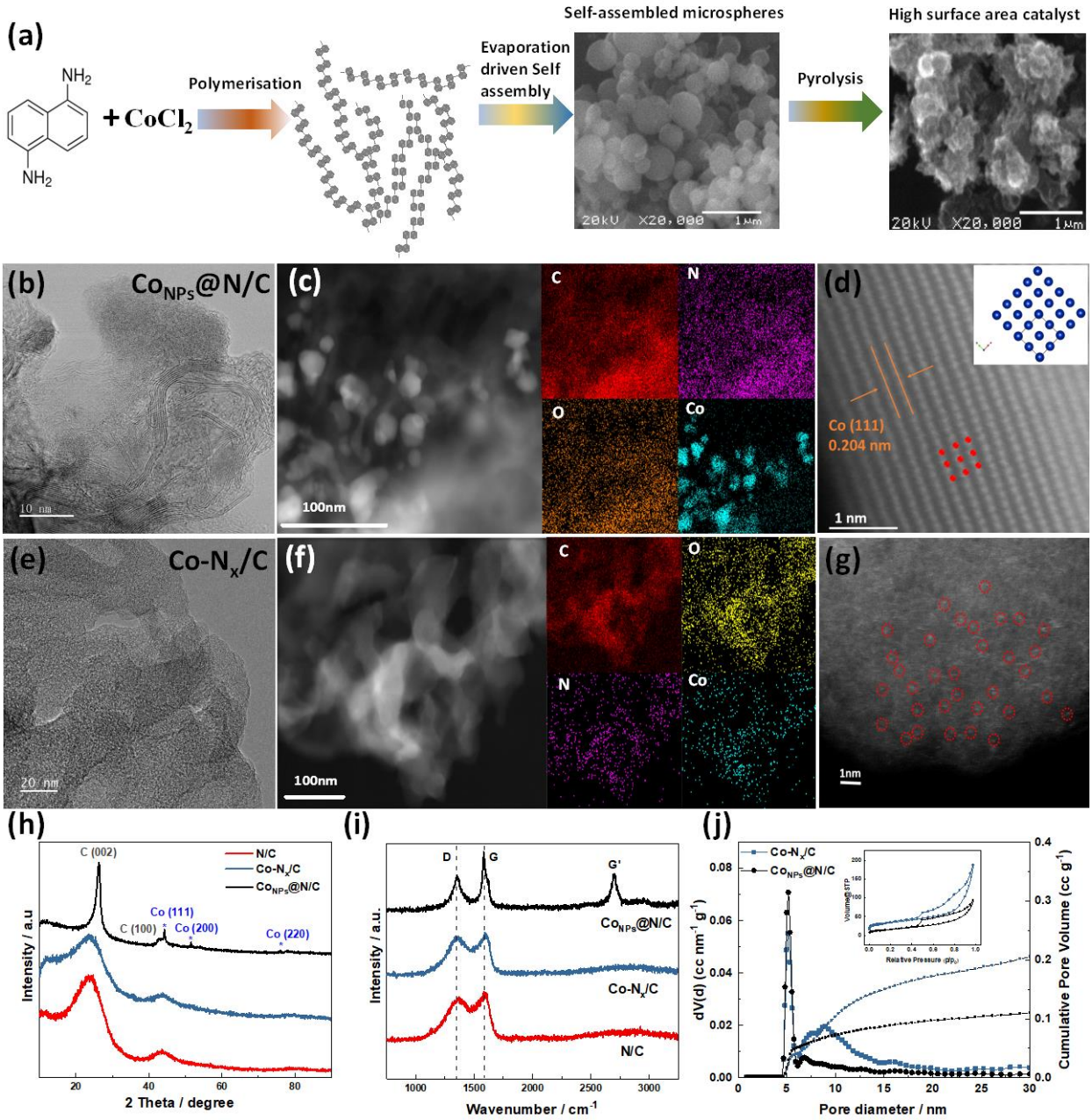

Figure 1 (a) Schematic of the catalyst synthesis process, and SEM images of the Co_{NPs}@N/C catalyst before and after pyrolysis. (b) High-resolution TEM images, (c) STEM-EDS mapping, and (d) HAADF-STEM image of the Co_{NPs}@N/C catalyst, inset is the crystal model on the [001] zone axis of metallic cobalt. (e) High-resolution TEM images, (f) STEM-EDS mapping, and (g) HAADF-STEM image of the Co-N_x/C catalyst. (h) XRD patterns and (i) Raman spectroscopy of the Co_{NPs}@N/C, Co-N_x/C, and N/C catalysts. (j) N_2 isotherms and corresponding pore size distribution of Co_{NPs}@N/C and Co-N_x/C catalysts.

3. Results and Discussion

The synthetic steps for the preparation of the Co_{NPs}@N/C catalyst are presented in Figure 1a. Catalyst precursors were synthesized in a one-pot process by dispersing 1,5-diaminonaphthalene and $CoCl_2$ in ethanol and stirring for 24 h. The mixture was then heated up to 80 ℃ to remove the solvent and complete

the polymerization. The morphologies of the precursor were firstly characterized by scanning electron microscopy (SEM) and these self-assembled nanospheres precursors were then pyrolyzed in a tube furnace at 1000 ℃ under an inert N_2 atmosphere for 2 h to obtain the Co_{NPs}@N/C catalyst. As shown in Figure 1a, high surface area carbon materials, with nitrogen and cobalt doped, were achieved after pyrolysis. Moreover, the Co-N_x/C catalyst was also synthesized as a comparison. In this synthesis, the pyrolysis temperature was decreased to 950℃ and ammonium persulfate was added during the polymerization step to promote the formation of oligomers.[21] Similarly, N/C catalyst was synthesized using the same method but no additional metal resource was added. The structural morphology of the Co_{NPs}@N/C and Co-N_x/C catalysts was further characterized by TEM. As shown in Figure 1b, high-resolution TEM image of the Co_{NPs}@N/C clearly show the lattice of graphitized carbon, as well as the morphology of porous carbon nanostructures and cobalt nanoparticles (Figure S1), with an average particle size of ~25 nm. The formation of porous carbon nanostructures might be caused by the removal of excessive cobalt nanoparticles by acid leaching. The STEM-EDS mapping in Figure 1c characterized the element composition and distribution of Co_{NPs}@N/C, further confirming the existence of metallic cobalt nanoparticles and uniform nitrogen doping. Furthermore, the lattice spacing (0.204nm) of face-centered cubic Co (111) crystal planes observed in the high-angle annular dark-field scanning transmission electron microscopy (HAADF-STEM) in Figure 1d identified the crystal structure of metallic cobalt nanoparticles. Conversely, as shown in Figure 1e and Figure 1f, no graphitized carbon and cobalt nanoparticles can be observed in the Co-N_x/C catalyst while certain amount of atomically dispersed Co atoms can be found in the HAADF-STEM image in Figure 1g. Additionally, the morphology of the metal-free N/C catalyst was also characterized by HRTEM (Figure S2). Moreover, as shown in Figure 1h, the XRD patterns exhibit two broad diffraction peaks for the N/C and Co-N_x/C catalysts at around 25°and 44°, which can be assigned to amorphous carbon. However, due to the presence of the Bragg reflection of the (002) peak at 25°, high crystallinity can be observed in the

Co_{NPs}@N/C catalyst, indicative of the formation of highly graphitized carbon. Besides, the three sharp peaks showed in the Co_{NPs}@N/C catalyst at 44°, 51°, and 76° can be assigned to the (111), (200), and (220) facets of metallic cobalt (PDF#15-0806), respectively. The above XRD data correspond well with the results observed by TEM. The existence of metallic cobalt indicates that some coordinated cobalt ions from cobalt chloride are reduced under reductive inner atmosphere and formed cobalt nanoparticles during the pyrolysis.[5] The trend in graphitization observed in XRD was also verified by Raman spectroscopy (Figure 1i). The peak located at 1365 cm^{-1} (D band) is attributed to disordered sp^3 carbon , whereas the peak located at 1584 cm^{-1} (G band) is related to graphitic sp^2-hybridized carbon.[20] The width of the Raman G and D bands increases in the order Co_{NPs}@N/C < N/C < Co-N_x/C, with an increased intensity ratio of D band to G band (I_D/I_G) from 0.83 for Co_{NPs}@N/C to 0.98 for Co-N_x/C, indicating increased tortuosity and defects of the graphene layers.[26] It can be observed that the N/C prepared without the addition of cobalt presents a highly disordered carbon while higher degree of graphitization was found in the Co_{NPs}@N/C, which can also be indicated by the 2D band located at ~2700 cm^{-1} for the Co_{NPs}@N/C due to the interaction between neighboring graphitic planes and the variations in the total number of graphene layers.[27] The porosity of the Co_{NPs}@N/C and Co-N_x/C was further investigated based on the N_2 adsorption / desorption isotherms, as shown in the inset of Figure 1j, both the isotherms are typical for mesoporous materials, with a hysteresis loop showing at high N_2 pressures.[28] The Brunauer-Emmett-Teller (BET) surface area of the Co-N_x/C (119.9 m^2 g^{-1}) is twice as much as that of Co_{NPs}@N/C (59.8 m^2 g^{-1}), indicating that the higher pyrolysis temperate resulting in the formation of highly graphitized carbon and hence less porous carbon. The pore size distribution (PSD) was determined according to the density function theory (DFT) model. Both the pore size distribution of the Co_{NPs}@N/C and Co-N_x/C focused at ~5.2 nm. However, the Co-N_x/C showed a slightly wider PSD ranging from 5 nm to 15 nm, which might contribute to the increased BET surface area of the Co-N_x/C. The results showed that the texture of these carbon-based materials depends significantly on the pyrolysis temperature.[29]

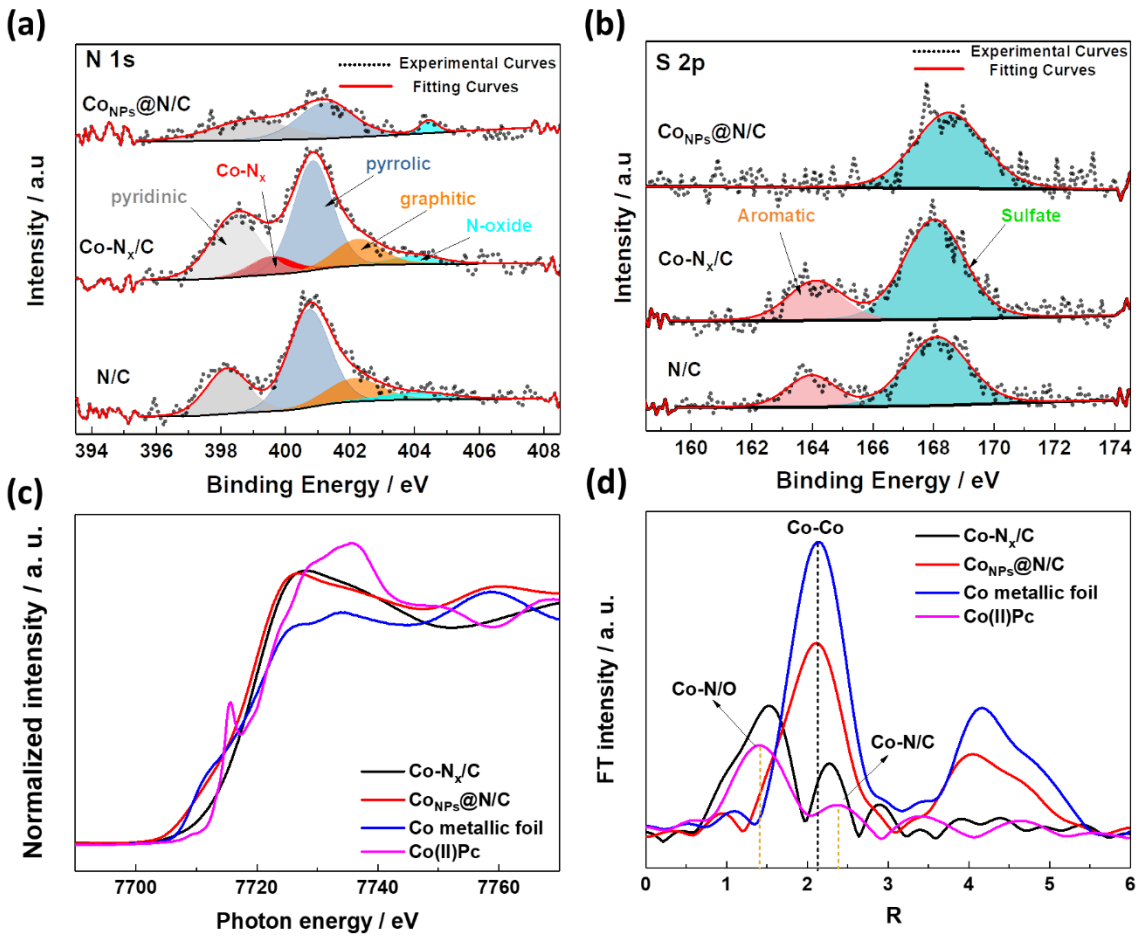

Figure 2 High-resolution (a) N 1s and (b) S 2p XPS spectra of the Co_{NPs}@N/C, Co-N_x/C, and N/C catalysts. (c) XANES and (d) EXAFS curves of the Co K edge of the Co_{NPs}@N/C and Co-N_x/C catalysts.

Furthermore, in order to gain further information about the surface elemental composition, X-ray photoelectron spectroscopy (XPS) was performed. The survey spectrum (Figure S3) revealed small amounts of Co in Co-N_x/C (~0.02 at%) and Co_{NPs}@N/C (~0.05 at%), lower than the contents of Co measured by ICP-AES in Co-N_x/C (0.16 at %) and Co_{NPs}@N/C (0.26 at %), suggesting that large amounts of Co in these two catalysts are in the bulk of carbon matrices. Besides, relatively high content of nitrogen was discovered on the surface of all the three samples (3.47 at% for N/C, 3.36 at% for Co-N_x/C, and 1.49 at% for Co_{NPs}@N/C). In the deconvoluted high resolution N 1s spectra (Figure 2a), the peaks located at 398.5 eV, 399.4 eV, 400.7 eV, 401.6 eV, and 405.2 eV are assigned to pyridinic, Co-N_x moieties, pyrrolic, graphitic, and N-oxide, respectively.[30-32] Details about the content of each nitrogen species in the catalysts can be found in Table S1. Moreover, as shown in the deconvoluted S 2p spectra in Figure 2b, two main peaks were observed in the Co-N_x/C and N/C catalysts. The broad peak located at

the binding energy of 164 eV can be attributed to aromatic sulfur or sulfones and thiophene due to the introduction of persulfate species for oxidative polymerization during the synthesis step.[33] The other peak at higher binding energy should be assigned to surface sulfate due to leaching with sulfuric acid.

In order to further investigate the valence state and local coordination environment of cobalt in the Co_{NPs}@N/C and Co-N_x/C, XANES and EXAFS spectra were obtained. As shown in Figure 2c by the Co K-edge XANES spectra, the adsorption edge profile of Co-N_x/C is between Co metallic foil and Cobalt (II) Phthalocyanine (CoPc), revealing that the Co in Co-N_x/C has an oxidation state between 0 and 2+. The nearly absence of a pre-edge feature at ~7709 eV in the Co-N_x/C catalyst suggests a symmetric coordination environment of Co, for example, Co-N_4.[34] In contrast, as for the Co_{NPs}@N/C, Co are quite visibly in the 0 oxidation state as its edge-position profile is much closer to Co metallic foil. Furthermore, the corresponding Fourier transforms of EXAFS for the Co_{NPs}@N/C and Co-N_x/C are plotted in Figure 2d. As for the Co_{NPs}@N/C catalyst, the signal at 2.14 Å matches well with the spectra of metallic cobalt foil, suggesting that these peaks are mainly from the Co-Co scattering in cobalt nanoparticles, Co_{NPs}. However, the Co-N_x/C catalyst exhibits two different peaks at 1.53 Å and 2.27 Å, which correspond to the Co-N/O and Co-N/C scattering pair, respectively.

The reactivity and selectivity of the catalysts towards ORR were assessed using the RRDE technique. In order to avoid active precious metal contamination (*e.g.* Pt), a glassy carbon rod was chosen as the counter electrode. The gold ring was held at +1.5 V_{RHE} to measure the amount of hydrogen peroxide formed at the disk electrode during the ORR. A gold ring is used (rather than Pt, which is often used in the literature) because oxygen evolution is poor on Au and allows a more stable H_2O_2 oxidation response at a higher potential. All the electrochemical results have had the response obtained under N_2 subtracted from them with one example found in Figure S5. Moreover, in order to investigate the effect of nitrogen doping, bare cobalt nanoparticles supported on carbon (denoted as Co_{NPs}/C) was prepared and tested as a comparison. The synthesis of Co_{NPs}/C is similar to that of Co_{NPs}@N/C, except that 1,5-diaminonaphtalene

was replaced by carbon black powder (Vulcan XC72R, Cabot). The physical characterizations for Co_{NPs}/C can be found in Figure S6-S8.

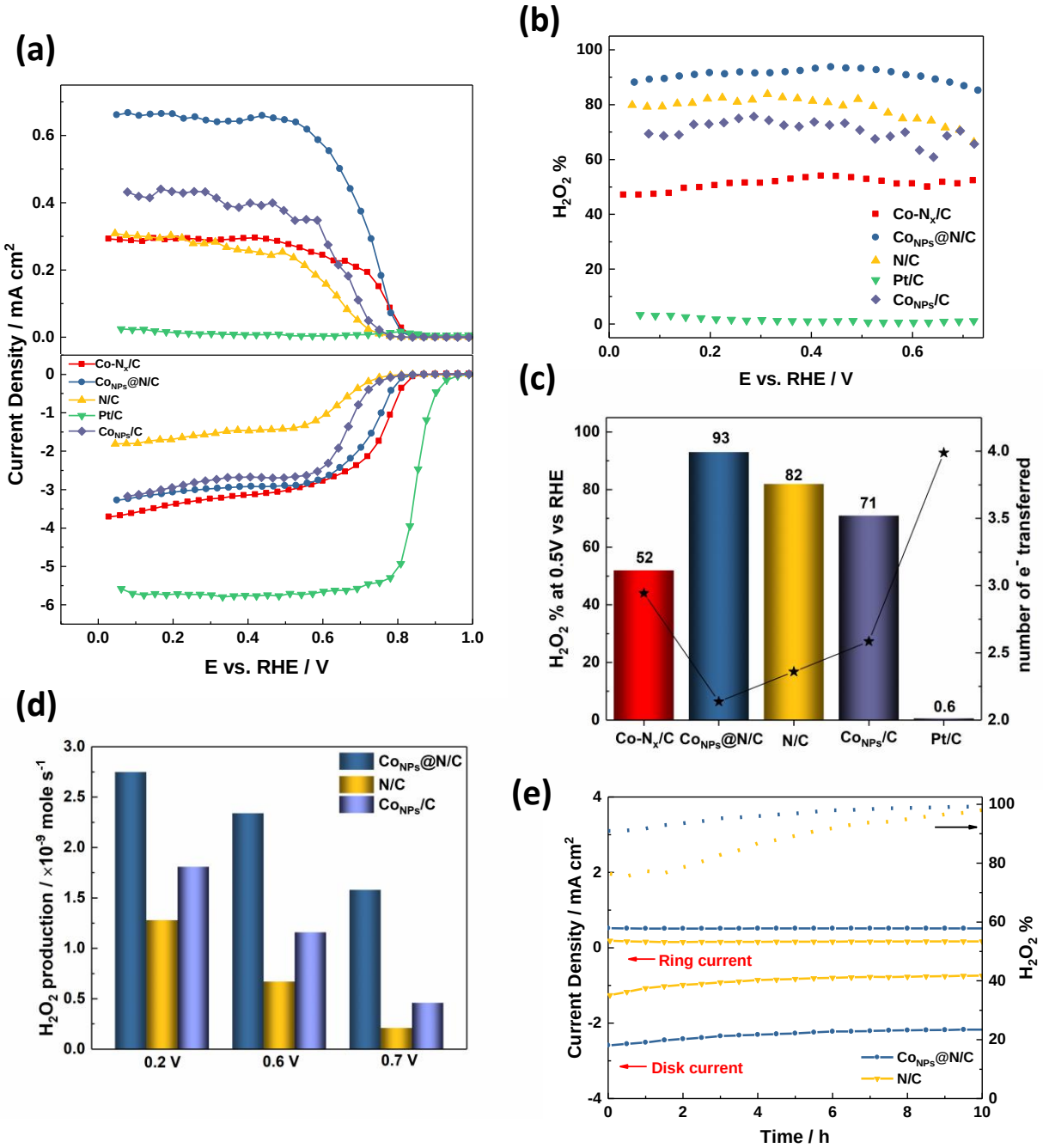

Figure 3 (a) Steady-state RRDE measurements in 0.1 M KOH, with the Au ring held at +1.5 V_{RHE}, rotating speed: 1600 rpm, 30 s hold, 30 mV step potential, catalysts loading: 100 μg cm^{-2}, Pt/C: 20 μg cm^{-2}. (b) H_2O_2 yield and (c) H_2O_2 selectivity (H_2O_2 %) and the corresponding electron transfer number at +0.5 V_{RHE} derived from RRDE data in Figure 3 (a). (d) Moles of H_2O_2 produced on the Co_{NPs}@N/C, N/C and Co_{NPs}/C electrocatalysts at different potential derived from RRDE data in Figure 3 (a). (e) Chronoamperometric response of the Co_{NPs}@N/C and N/C electrocatalyst at 0.6 V for stability evaluation.

Figure 3a shows the ORR disk current (lower panel) while the ring current (upper panel) monitors H_2O_2 production. The Co_{NPs}@N/C catalyst exhibits high activity for ORR with an onset potential of 0.85 V

(defined as the potential at the current density of 0.01 mA cm^{-2})[35] versus RHE. The potential to drive a current density of 1.0 mA cm^{-2} is 0.76 V versus RHE, which is significantly higher than those for the previously reported catalysts (Table S2). As shown in Figure 3b and Figure 3c, the Pt/C shows a typical $4e^-$ process towards the oxygen reduction with the lowest H_2O_2 selectivity (~ 1%) and the highest electron transfer number being measured. The Co_{NPs}@N/C catalyst delivers the highest H_2O_2 selectivity in a wide potential range of 0.05-0.75 V versus RHE. Note that an H_2O_2 yield of 93% at 0.5 V versus RHE was achieved and the corresponding electron transfer number is estimated to be 2.13. Without the addition of cobalt nanoparticles, the N/C electrocatalyst demonstrates poorer ORR reactivity compared with Co_{NPs}@N/C, as a lower potential of 0.61 V versus RHE at 1.0 mA cm^{-2} are observed, suggesting that the synergy of cobalt nanoparticles is crucial to the reactivity towards ORR. However, interestingly, although it has the lowest ORR reactivity, the selectivity for the electrosynthesis of H_2O_2 on N/C is high, with 82 % obtained at 0.5 V versus RHE. As for the Co-N_x/C, the highest ORR reactivity is achieved among all the aforementioned carbon-based catalysts prepared in this work verified by the highest potential of 0.78 V versus RHE at 1.0 mA cm^{-2}, and this is coupled with the lowest H_2O_2 selectivity with 52% of H_2O_2 yield and corresponding electron transfer number of 3.01 observed at 0.5 V versus RHE. In contrast, Co nanoparticles deposited on carbon which does not contain significant nitrogen functionality (Co_{NPs}/C) was also tested to investigate the effect of nitrogen doping in the substrate towards oxygen reduction. As shown in Figure 3a, the Co_{NPs}/C catalyst delivers a 1 mA cm^{-2} current density at only 0.67 V versus RHE. Besides, slightly lower H_2O_2 selectivity is found on Co_{NPs}/C over a wide potential range of 0.05-0.75 V versus RHE compared with the N/C catalysts. The comparatively high selectivity of the Co_{NPs}/C catalysts might result from the formation of Co-C-O motifs in the Co_{NPs}/C catalysts analogous to the previously reported Fe-C-O motifs, which are highly active towards the electrosynthesis of H_2O_2 in alkaline solutions.[36] Additionally, the effect of sulfur doping on the ORR activity was investigated based on previous work in the group by changing the sulfur containing ammonium persulfate to H_2O_2, but no

significant difference in the ORR performance in the presence or absence of sulfur was found.[37] As mentioned above, although the H_2O_2 selectivity on the metal-free N/C and Co_{NPs}/C is considerably high, however, if molar production of H_2O_2 molecule on these catalysts was considered, the Co_{NPs}@N/C catalysts showed significantly better performance than the metal-free N/C and Co_{NPs}/C. For instance, production of H_2O_2 increases almost 8-fold from 0.21 (N/C), and 4-fold from 0.46 (Co_{NPs}/C) to 1.58 (Co_{NPs}@N/C) × 10^{-9} mole s^{-1} at 0.7 V versus RHE. Besides, different transition metal nanoparticle catalysts supported on nitrogen doped carbon, M_{NPs}@N/C (M= Fe, Ni, and Cu), were prepared through the same synthesis as the Co_{NPs}@N/C, except for the use of different metal source (e.g. $FeCl_2$). The ORR results (Figure S9) reveal the trend in H_2O_2 yield as Co_{NPs}@N/C > Ni_{NPs}@N/C > Cu_{NPs}@N/C ≈ Fe_{NPs}@N/C, indicating the most favorable two electron selectivity towards ORR for producing H_2O_2 over the Co_{NPs}@N/C catalyst. The above electrochemical tests towards the electrosynthesis of H_2O_2 on the as-prepared four carbon-based electrocatalysts demonstrate that the synergy of cobalt nanoparticles and nitrogen doping play an essential role in both accelerating the reactivity of oxygen reduction and improving the H_2O_2 selectivity. Moreover, the performance stability of the N/C and Co_{NPs}@N/C catalysts were also evaluated by the chronoamperometry test at a fixed disk potential of 0.6 V verse RHE. As shown in Figure 3e, the apparent increase of ring current and H_2O_2 selectivity on both the N/C and Co_{NPs}@N/C catalysts should be attributed to the gradual accumulation of H_2O_2 in the electrolyte. The concentration of generated H_2O_2 was also determined using a colorimetric method (Section S9 and S10). With an applied potential of 0.6 V_{RHE} and using 100mL electrolyte, after 10 h reaction a typical concentration of H_2O_2 is about 0.76 mM, with a Faradaic efficiency of ~82%, corresponding to a H_2O_2 production rate of ~3.8mol_{H2O2} g_{Co}^{-1} h^{-1}. After changing the electrolyte, high H_2O_2 selectivity of ~ 90% on the Co_{NPs}@N/C catalyst can be recovered (Figure S10). X-Ray Fluorescence analysis (XRF) was performed on the electrolyte after the 10 h reaction to examine possible cobalt species in the solution, as shown in Figure S13 and Table S3, with no detectable cobalt observed in the electrolyte.

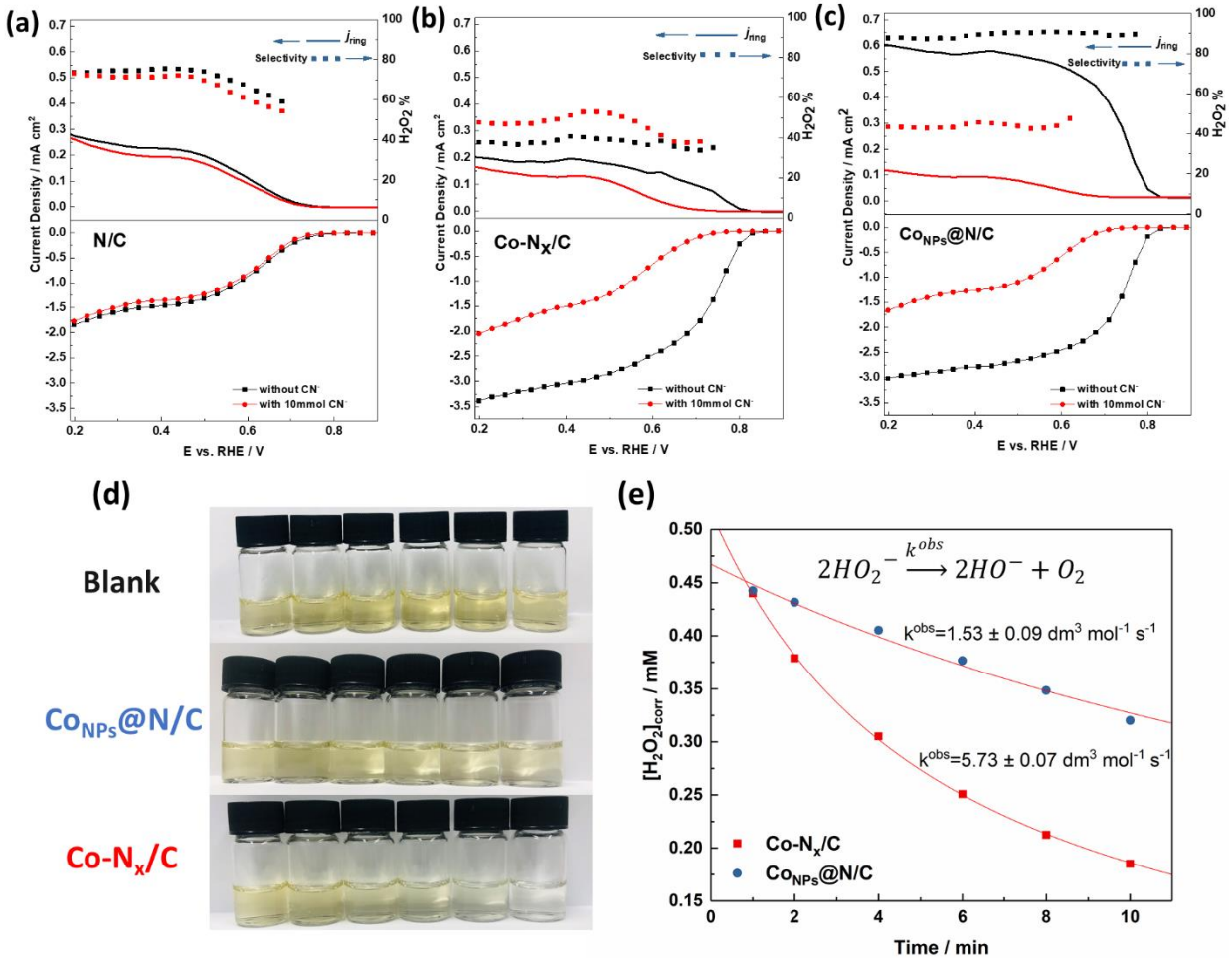

Figure 4 Steady-state RRDE measurements of the (a) N/C, (b) Co-N_x/C, and (c) Co_{NPs}@N/C catalysts in 0.1 M KOH with and without 10mmol KCN, with the Au ring held at +1.5 V_{RHE}, rotation frequency: 1600 rpm, 30 s hold, 30 mV step potential, catalysts loading: 100 µg cm^{-2}. (d) Catalytic decomposition of H_2O_2 with time (time increases going from left to right hand side) in the presence and absence of Co_{NPs}@N/C and Co-N_x/C catalysts. Aliquots from the reaction mixture were extracted, filtered and reacted with 0.1 M $TiOSO_4$ solution to produce a yellow colored peroxy titanium (IV) (see section S9 for discussion). (e) Background corrected H_2O_2 concentration versus time during disproportionation of hydrogen peroxide in the presence of Co_{NPs}@N/C and Co-N_x/C catalysts. Also shown is the fit to a 2nd order decomposition process and the derived rate constants. Solution composition: 0.1 M KOH, 0.5 mM H_2O_2, 1 mg dm^{-3} catalyst.

The distinct functions of the Co_{NPs}@N/C and Co-N_x/C were further investigated by selectively poisoning one type of metal center at a time and then monitor changes in ORR reactivity and selectivity.[25] It has been known that cyanide ions (CN^-) can coordinate with transition metals such as Fe and Co, resulting in inhibiting metal active sites toward ORR and hence decreasing the ORR activity.[38-39] For comparison, the ORR activity of the Co-free nitrogen containing carbon substrate (N/C) was also determined. The ORR activity of the aforementioned electrocatalysts was compared in O_2-saturated 0.1M KOH in the presence

or absence of 10mM KCN in order to investigate the essential role of metal active sites for the ORR. As shown in Figure 4a, addition of CN^- has no effect on the N/C carbon substrate. In contrast, the introduction of CN^- to the Co containing catalysts resulted in impaired ORR reactivity on both the Co_{NPs}@N/C and Co-N_x/C by shifting ORR polarization curves towards negative potentials, Figure 4b and c. Indeed, the performance as characterized by the disk current of the Co_{NPs}@N/C and Co-N_x/C catalysts after poisoning look very similar to that of the N/C catalysts suggesting that the Co has been very effectively poisoned leaving only the activity of the underlying support material. Similarly, the ring currents after poisoning of the Co-containing catalysts look similar in terms of shape and magnitude (although maybe slightly less in magnitude) compared to the N/C catalyst. Small differences in the poisoned activity suggest that there might be some residual (i.e. non-poisoned) activity on the Co catalysts, although the effect is small. Although the Co-N_x/C catalyst showed a significant decrease in disk current and negative shift in potential, the selectivity of its ORR does not significantly change. In contrast, there is a significant drop in the H_2O_2 selectivity for the Co_{NPs}@N/C catalyst upon CN^- poisoning which seems mainly associated with the lower selectivity of H_2O_2 production on the underlying N/C support i.e. the selectivity which would be composed of the selectivity's of the reaction on both Co_{NPs}@N/C and N/C and which upon poisoning becomes dominated by the N/C selectivity.

In order for a catalyst to be effective at production of hydrogen peroxide, three independent factors need to be fulfilled: a) Reduction of oxygen to peroxide should be a facile and easy process; b) the produced peroxide should not be bound too tightly to the catalyst site, so that it can desorb from the catalyst rather than continue to be reduced to water; and c) the disproportionation reaction of the generated hydrogen peroxide needs to be suppressed. Reduction of oxygen to the hydrogen peroxide anion occurs at a slightly higher potential than the equivalent potential in acid due to the added stability of the hydrogen peroxide anion in alkaline solution (hydrogen peroxide is a weak acid with a pK_a of 11.7 [40])

$$O_2 + H_2O + 2e^- \rightleftarrows HO^- + HO_2^- \qquad E^o(O_2, HO_2^-)=-0.065V \quad E^{RHE}(O_2,HO_2^-)=0.761\ V \qquad (4)$$

$$O_2 + 2H^+ + 2e^- \rightleftarrows H_2O_2 \qquad E^o(O_2, H_2O_2)=0.695\ V \quad E^{RHE}(O_2,H_2O_2)=0.695\ V \qquad (5)$$

where the potentials are calculated from the thermodynamic data in [40]. The onset potential for the ORR on both Co_{NPs}@N/C and Co-N_x/C seem well aligned this potential. The disproportionation of hydrogen peroxide is a highly favorable process having a large and negative free energy change in alkaline environment[40]

$$2HO_2^- \rightarrow 2HO^- + O_2 \qquad \Delta_rG=-176.86 \text{ kJ mol}^{-1} \qquad (6)$$

In order to understand whether the high selectivity seen towards H_2O_2 production on the Co_{NPs}@N/C catalyst compared to the Co-N_x/C is related to catalysis of the disproportionation reaction (i.e. point c, equation 6 above), we examined the ability of each of the catalysts to catalyze the disproportionation reaction of 0.5 mM H_2O_2 in a chemical reaction, Figure 4 (d) and (e) (see experimental section 3.4). Filtered aliquots of the reactant mixture were reacted with $TiOSO_4$ solution in order to produce a colored peroxy-titanium(IV) complex. Figure 4(d) shows that aliquots taken at progressively longer time decrease in color intensity as the amount of hydrogen peroxide decreases. Figure 4(e) shows the change in H_2O_2 concentration with time (see supplementary section 9 for calibration). The response curves are well described by a 2nd order process i.e.

$$\frac{d[HO_2^-]}{dt} = k_{obs}[HO_2^-]^2 \qquad [HO_2^-]_t = \frac{1}{k_{obs}t + \frac{1}{[HO_2^-]_0}} \qquad (7)$$

although the Co_{NPs}@N/C catalyst also shows reasonable fits for zeroth and first order decays. k_{obs} for the Co-N_x/C is significantly higher than on the Co_{NPs}@N/C catalyst suggesting that the hypothesis that lower H_2O_2 yield on Co-N_x/C is associated with faster H_2O_2 decomposition is reasonable.

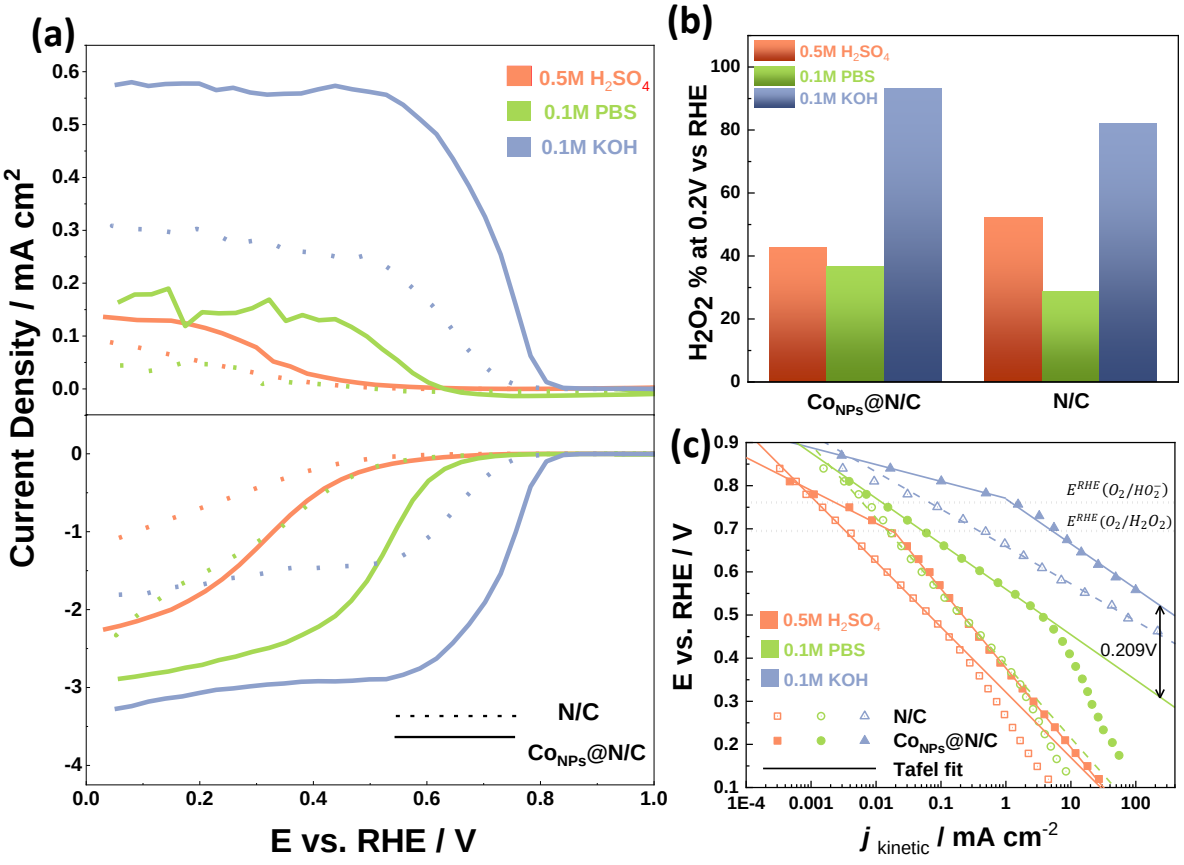

Figure 5 (a) Steady-state RRDE measurements of the Co_{NPs}@N/C and N/C catalysts in 0.1 M KOH, 0.5 M H_2SO_4, and 0.1 M PBS, respectively, with the Au ring held at +1.5 V_{RHE}, rotating speed: 1600 rpm, 30 s hold, 30 mV step potential, catalysts loading: 100 μg cm^{-2}. (b) H_2O_2 selectivity (H_2O_2 %) at +0.2 V_{RHE} and (c) Tafel plot derived from RRDE data in Figure 5(a).Tafel lines fit over at least 2 ½ orders of magnitude of current with parameters collected in Table 1, $E^{RHE}(O_2,HO_2^-)$=0.761 V and $E^{RHE}(O_2,H_2O_2)$=0.695 V equation 4 and 5.

The electrolyte pH effect for H_2O_2 production over both the Co_{NPs}@N/C, N/C, and Co-N_x/C (Figure S14) catalysts were also investigated, with three different electrolytes covering strongly alkaline, neutral pH, and strongly acidic conditions. As shown in Figure 5a and Table 1 the onset potential of oxygen reduction for Co_{NPs}@N/C and N/C catalysts decrease with decreasing pH with the Co_{NPs}@N/C catalyst always having a higher onset potential than the N/C catalyst. The shifts in onset potential on moving from pH 13 to pH 7.2 on the N/C and Co_{NPs}@N/C catalysts (0.07 V, 0.09 V, respectively), are quite close to the shift in equilibrium potential in moving from HO_2^- to H_2O_2 as product (0.066V). For N/C catalyst this shift seems entirely due to the shift in the equilibrium potential whereas for the Co_{NPs}@N/C catalyst there is liable to be some mechanistic change also adding a contribution. In acid solution, there is a further

negative shift in the onset potential for both catalysts, and it is reasonable to assume that this is due to a mechanistic change in the reduction process.

Table 1. Onset potential and Tafel analysis of results in Figure 5 as a function of catalyst, electrolyte (pH) and (for the Co_{NPs}@N/C catalyst) potential range. The potential range over which the Tafel slope was measured was either above or below the standard potential for oxygen reduction to the peroxide anion ($E^{RHE}(O_2,HO_2^-)$=0.761 V, pH>11.7) or hydrogen peroxide ($E^{RHE}(O_2,H_2O_2)$=0.695 V, pH<11.7) respectively.

Electrolyte	pH	Catalyst				
		N/C		Co_{NPs}@N/C		
		E_{onset} /V	Tafel slope / mV decade^{-1}	E_{onset} /V	Tafel slope, $E > E^{rev}_{O_2,H_2O_2}$ / mV decade^{-1}	Tafel slope, $E < E^{rev}_{O_2,H_2O_2}$ / mV decade^{-1}
0.1 M (KOH)	13	0.81	86	0.85	39	104
0.1M PBS	7.2	0.74	170	0.76	N.A	105
0.5 M H_2SO_4	0.3	0.61	151	0.71	76	184

Tafel analysis was then performed to investigate the ORR kinetics in these electrolytes as a function of pH using the Tafel equation:[41]

$$\eta = a \log j + b \tag{8}$$

where η is the overpotential, j is the kinetic current density, and a is the Tafel slope. The kinetic current densities were calculated based on the Koutecky-Levich equation:[42]

$$1/j_{kin} = 1/j_{disk} + 1/j_{lim} \tag{9}$$

where j_{disk} and j_{lim} are the current density measured on the disk and the current density due to diffusion limitation, respectively. It should be noted that the disk current density value at 0 V_{RHE} was taken as the diffusion-limited current density for the N/C catalyst in acidic and neutral solutions, as well as the Co_{NPs}@N/C catalyst in acid, since there is no obvious diffusion limitation being reached for the aforementioned results under the selected potential range. Tafel analysis is somewhat complicated by the possibility of two different products, although we assume that the reactions are dominated by oxygen

reduction to hydrogen peroxide as confirmed by the measured peroxide yield on these materials. In order to establish a pseudo-steady state performance for the catalysts in Tafel analysis each measurement point was polarized for 30s during which time the current stabilized.

Figure 5c, shows the kinetic currents for the N/C and Co_{NPs}@N/C catalysts as a function of pH and with Tafel slopes (lines) calculated over appropriate ranges of current. Tafel slopes were only calculated where there was at least 2½ orders of magnitude of current showing a linear trend and in all cases the correlation coefficients were greater than 0.984 (average 0.994, n=8). Table 1 collects the parameters from the Tafel analysis. The Co_{NPs}@N/C catalyst shows two different Tafel slopes whereas the N/C catalyst in general only shows one slope. A summary of the slopes is provided in Table 1 and show gradually increased Tafel slopes as the pH of the electrolyte decreases, reflecting the retardation of ORR kinetics.

Interestingly, the Co_{NPs}@N/C catalyst shows two different Tafel slopes, with the two Tafel lines intersecting each other very close to the equilibrium potentials for oxygen reduction to peroxide in the respective electrolyte ($E^{RHE}(O_2,HO_2^-)$=0.761 V, in 0.1 M KOH and $E^{RHE}(O_2,H_2O_2)$=0.695 V, in 0.5 M H_2SO_4). This suggest that the Tafel slopes at higher potential are due to the ORR forming water and this then switches to peroxide generation once the potential falls below the equilibrium potential for that reaction. Note that limited data for the 0.1 M PBS case does not allow fitting of 2nd Tafel slope for the catalyst in that electrolyte. In the high potential region, the Tafel slopes are quite low, 39 and 76 mV decade^{-1} in alkaline and acid, respectively. Such a low value of Tafel slope is often seen during oxygen reduction on platinum in the so-called “oxide region” and is typically ascribed to surface coverage effects – that is it is not indicative of a reaction which accelerates very quickly with applied overpotential, but rather associated with more reaction sites becoming available as the potential is reduced.

For Co nanoparticles, it is reasonable to consider which species may exist on the surface during the oxygen reduction reaction over the potential ranges which are accessed, as the surface speciation may be important in directing the reaction. Indeed, Co has a rather rich (electro)chemistry in alkaline and neutral

pH environments, and in principle multiple solid state species comprising Cobalt in the +2, (+2/+3 mixed) and +3 ($CoO/Co(OH)_2$, Co_3O_4, $Co_2O_3/CoOOH$) oxidation states may exist as a function of pH and potential in our experiments as shown by its Pourbaix diagram[43]. In acid conditions, only Co^{2+} exists as the stable species over the electrochemical potentials accessed by our experiments, although Pourbaix points out that in non-oxidizing acids Cobalt is found to be quite (kinetically) stable because of its large overpotential towards the hydrogen reaction. The potential range over which this low Tafel slope occurs – 0.75-0.85 V (RHE) in alkaline environment is close to the expected potential for the reduction of Co_3O_4 to CoO[43]

$$Co_3O_4 + H_2O + 2e^- \rightleftharpoons 3CoO + 2OH^- \qquad E^o=-0.051V \qquad E^{RHE}=0.777\ V \quad (9)$$

Thus in the high potential region on the Co nanoparticles, the low Tafel slope appears to be associated with the increase in number of available CoO sites as the potential is decreased. This suggests that $CoO/Co(OH)_2$ is probably the active site for oxygen reduction in alkaline/neutral environments. Once the applied potential decreases below the hydrogen peroxide equilibrium potential, the reaction switches to peroxide production. In alkaline and neutral environments, the Tafel slope on the Co_{NPs}@N/C catalyst is almost identical at 104 and 105 mV $decade^{-1}$ - slightly less than the 118 mV $decade^{-1}$ expected for a one electron RDS with transfer coefficient of ½. The similarity of the Tafel slopes suggest that the mechanism remains the same on the catalyst as the pH is changed, but an extra 209 mV overpotential is required to drive the oxygen reduction at the same rate. As the potentials are measured versus the RHE, this difference is not due to a reference electrode effect but must be associated with a difference in the reaction. Part of the extra 209 mV overpotential is associated with the different products formed: H_2O_2 at pH 7.2 and HO_2^- at pH 13, but the associated shift of equilibrium potential by 66 mV (equation 4&5) only accounts for part of the equilibrium potential. It is likely that the other component of the extra overpotential is associated with changes to the Co surface with pH associated with the coverage of $Co(OH)_2$ in alkaline conditions compared to CoO in more neutral and acidic conditions. In acid the

surface becomes more metal like and the reaction undergoes further mechanistic changes and the Tafel slope becomes even larger suggesting a more kinetically hindered reaction. Hence we suggest that the favored mechanism within alkaline and neutral environments follows the following scheme 1 on cobalt nanoparticle catalysts

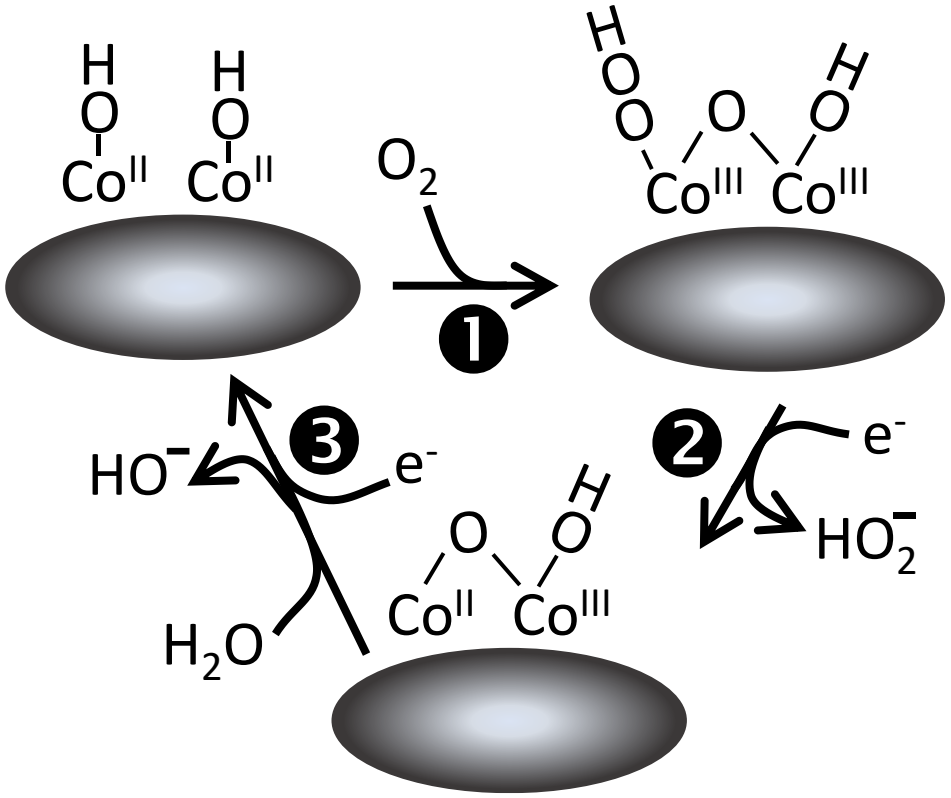

Scheme 1 Mechanistic process for the reduction of oxygen to hydrogen peroxide

The oxidation of $Co(OH)_2$ by oxygen (step 1) is a process known to occur in aqueous and alkaline solutions[44], and although we write it as a single step, it might involve a number of intermediate steps involving, for instance, the initial formation of a bound superoxide species prior to proton transfer to produce the bound peroxide species. However, a crucial process in electrochemical step 1 is the proton transfer from an adjacent OH to the bound superoxide species. In step 2, reduction of one of the Co(III) sites leads to loss of the peroxide anions, and subsequent reduction of the remaining Co(III) and proton abstraction from water in step 3 leads to regeneration of the surface. The potential of the electrochemical reduction of Co(III) oxides in steps 2 and 3 are well aligned with the reduction potentials of cobalt (III) oxides[40]. At low pHs, CoO is the preferred oxide form and so the surface concentration of OH on Co

decreases as pH is decreased leading to a loss in activity towards oxygen reduction as step 1 becomes more hindered.

4. Conclusion

In summary, four different carbon-based electrocatalysts, i.e. metal-free nitrogen-doped carbon, atomically dispersed Co-N_x/C, cobalt nanoparticles supported on bare carbon, and cobalt nanoparticles supported on nitrogen-doped carbon, were successfully prepared. The catalytic performance for H_2O_2 electrosynthesis of these four electrocatalysts were evaluated. Among them, the cobalt nanoparticles supported on nitrogen-doped carbon, namely Co_{NPs}@N/C, exhibited a good selectivity for a $2e^-$ pathway reduction of O_2 to H_2O_2 over 90% in a wide potential range of 0.05-0.75 V versus RHE), as well as good electrochemical stability in in 0.1M KOH electrolyte. We find that good performance for hydrogen peroxide generation is not only associated with good activity towards two electron reduction fo oxygen to hydrogen peroxide, but also associated with **poor** activity towards the hydrogen peroxide disproportionation reaction. The high selectivity towards H_2O_2 on the Co_{NPs}@N/C catalysts appears to be associated with not only a good activity for the peroxide production process, but also a significantly reduced activity towards the hydrogen peroxide disproportionation reaction compared to the Co-N_x/C tested. Tafel analysis of the most active catalysts provides details of the limiting process and we see that pH changes likely affect the surface composition of the catalyst and thus modify the performance. Conditions which favor the formation of OH covered surfaces (i.e. high pH) appear more favorable for reduction of oxygen to hydrogen peroxide. At intermediate or low pH, the formation of oxide covered surfaces reduce the activity towards hydrogen peroxide generation.

ASSOCIATED CONTENT

The supporting Information is available free of charge at….

The supporting information includes high resolution TEM and XPS of Co_{NPs}@N/C, Co-N_x/C , N/C and Co_{NPs}/C catalysts; Investigation of metal effect and pH effect towards ORR; Steady-state RRDE measurements of the Co_{NPs}@N/C before and after 10h chronoamperometry test; Colorimetric quantification of H_2O_2.

AUTHOR INFORMATION

Corresponding Author

*E-mail: anthony@imperial.ac.uk

ORCID:

Jun Wu: 0000-0002-7067-6917
Asad Mehmood: 0000-0001-8744-1105
Guohui Zhang: 0000-0003-3095-2689
Ghulam Ali: 0000-0003-2815-6667
Anthony Kucernak:0000-0002-5790-9683

Notes

The authors declare no competing financial interest.

Acknowledgements

Jun Wu would like to thank the China Scholarship Council and Imperial College London for the IC-CSC joint scholarship to support his PhD research. This research has been supported by the U.K. Engineering and Physical Sciences Research Council under project EP/J016454/1. We would also like to thank Dr. Shaoliang Guan from the Harwell EPSRC National XPS Facility for XPS analysis, Dr. Quentin Ramasse from SuperSTEM laboratory for HRTEM service and Dr. Hui Luo from

Imperial College London for BET analysis. The data used in the production of the figures in this paper are available to download at DOI: [DOI inserted during proofing stage].

References

1. Liu, Y.; Quan, X.; Fan, X.; Wang, H.; Chen, S.,High-Yield Electrosynthesis of Hydrogen Peroxide from Oxygen Reduction by Hierarchically Porous Carbon, *Angewandte Chemie - International Edition,* **2015,** 54, 6837-6841.
2. Murray, A. T.; Voskian, S.; Schreier, M.; Hatton, T. A.; Surendranath, Y.,Electrosynthesis of Hydrogen Peroxide by Phase-Transfer Catalysis, *Joule,* **2019,** 3, 2942-2954.
3. Wang, W.; Hu, Y.; Liu, Y.; Zheng, Z.; Chen, S.,Self-Powered and Highly Efficient Production of H2o2 through a Zn-Air Battery with Oxygenated Carbon Electrocatalyst, *ACS Applied Materials and Interfaces,* **2018,** 10, 31855-31859.
4. Zhang, Q.; Tan, X.; Bedford, N. M.; Han, Z.; Thomsen, L.; Smith, S.; Amal, R.; Lu, X.,Direct Insights into the Role of Epoxy Groups on Cobalt Sites for Acidic H2o2 Production, *Nature Communications,* **2020,** 11, 1-11.
5. Li, B. Q.; Zhao, C. X.; Liu, J. N.; Zhang, Q.,Electrosynthesis of Hydrogen Peroxide Synergistically Catalyzed by Atomic Co–Nx–C Sites and Oxygen Functional Groups in Noble-Metal-Free Electrocatalysts, *Advanced Materials,* **2019,** 31, 1808173.
6. Wu, K.-H.; Wang, D.; Lu, X.; Zhang, X.; Xie, Z.; Liu, Y.; Su, B.-J.; Chen, J.-M.; Su, D.-S.; Qi, W.; Guo, S.,Highly Selective Hydrogen Peroxide Electrosynthesis on Carbon: In Situ Interface Engineering with Surfactants, *Chem,* **2020,** 6, 1443-1458.
7. Edwards, J. K.; Solsona, B.; N, E. N.; Carley, A. F.; Herzing, A. A.; Kiely, C. J.; Hutchings, G. J.,Switching Off Hydrogen Peroxide Hydrogenation in the Direct Synthesis Process, *Science,* **2009,** 323, 1037-1041.
8. Iglesias, D.; Giuliani, A.; Melchionna, M.; Marchesan, S.; Criado, A.; Nasi, L.; Bevilacqua, M.; Tavagnacco, C.; Vizza, F.; Prato, M.; Fornasiero, P.,N-Doped Graphitized Carbon Nanohorns as a Forefront Electrocatalyst in Highly Selective O2 Reduction to H2o2, *Chem,* **2018,** 4, 106-123.
9. Jirkovský, J. S.; Panas, I.; Ahlberg, E.; Halasa, M.; Romani, S.; Schiffrin, D. J.,Single Atom Hot-Spots at Au-Pd Nanoalloys for Electrocatalytic H 2o 2 Production, *Journal of the American Chemical Society,* **2011,** 133, 19432-19441.
10. Lu, Z.; Chen, G.; Siahrostami, S.; Chen, Z.; Liu, K.; Xie, J.; Liao, L.; Wu, T.; Lin, D.; Liu, Y.; Jaramillo, T. F.; Nørskov, J. K.; Cui, Y.,High-Efficiency Oxygen Reduction to Hydrogen Peroxide Catalysed by Oxidized Carbon Materials, *Nature Catalysis,* **2018,** 1, 156-162.
11. Thostenson, J. O.; Ngaboyamahina, E.; Sellgren, K. L.; Hawkins, B. T.; Piascik, J. R.; Klem, E. J. D.; Parker, C. B.; Deshusses, M. A.; Stoner, B. R.; Glass, J. T.,Enhanced H2o2 Production at Reductive Potentials from Oxidized Boron-Doped Ultrananocrystalline Diamond Electrodes, *ACS Applied Materials and Interfaces,* **2017,** 9, 16610-16619.
12. Yang, S.; Verdaguer-Casadevall, A.; Arnarson, L.; Silvioli, L.; Čolić, V.; Frydendal, R.; Rossmeisl, J.; Chorkendorff, I.; Stephens, I. E. L.,Toward the Decentralized Electrochemical Production of H2o2: A Focus on the Catalysis, *ACS Catalysis,* **2018,** 8, 4064-4081.
13. Yi, Y.; Zhou, J.; Guo, H.; Zhao, J.; Su, J.; Wang, L.; Wang, X.; Gong, W.,Safe Direct Synthesis of High Purity H2o2 through a H2/O2 Plasma Reaction, *Angew Chem Int Ed Engl,* **2013,** 52, 8446-9.
14. Kim, D.; Nam, H.; Cho, Y. H.; Yeo, B. C.; Cho, S. H.; Ahn, J. P.; Lee, K. Y.; Lee, S. Y.; Han, S. S.,Unlocking the Potential of Nanoparticles Composed of Immiscible Elements for Direct H2o2 Synthesis, *ACS Catalysis,* **2019,** 9, 8702-8711.
15. Siahrostami, S.; Verdaguer-Casadevall, A.; Karamad, M.; Deiana, D.; Malacrida, P.; Wickman, B.; Escudero-Escribano, M.; Paoli, E. A.; Frydendal, R.; Hansen, T. W.; Chorkendorff, I.; Stephens, I. E. L.; Rossmeisl, J.,Enabling Direct H2o2 Production through Rational Electrocatalyst Design, *Nature Materials,* **2013,** 12, 1137-1143.

16. Verdaguer-Casadevall, A.; Deiana, D.; Karamad, M.; Siahrostami, S.; Malacrida, P.; Hansen, T. W.; Rossmeisl, J.; Chorkendorff, I.; Stephens, I. E. L.,Trends in the Electrochemical Synthesis of H2o2: Enhancing Activity and Selectivity by Electrocatalytic Site Engineering, *Nano Letters,* **2014,** 14, 1603-1608.
17. Wang, Y. L.; Gurses, S.; Felvey, N.; Boubnov, A.; Mao, S. S.; Kronawitter, C. X.,In Situ Deposition of Pd During Oxygen Reduction Yields Highly Selective and Active Electrocatalysts for Direct H2o2 Production, *ACS Catalysis,* **2019,** 9, 8453-8463.
18. Li, L.; Tang, C.; Zheng, Y.; Xia, B.; Zhou, X.; Xu, H.; Qiao, S. Z.,Tailoring Selectivity of Electrochemical Hydrogen Peroxide Generation by Tunable Pyrrolic-Nitrogen-Carbon, *Advanced Energy Materials,* **2020,** 10, 2000789.
19. Tang, C.; Jiao, Y.; Shi, B.; Liu, J. N.; Xie, Z.; Chen, X.; Zhang, Q.; Qiao, S. Z.,Coordination Tunes Selectivity: Two-Electron Oxygen Reduction on High-Loading Molybdenum Single-Atom Catalysts, *Angew Chem Int Ed Engl,* **2020,** 59, 9171-9176.
20. Wang, Y.; Shi, R.; Shang, L.; Waterhouse, G. I. N.; Zhao, J.; Zhang, Q.; Gu, L.; Zhang, T.,High-Efficiency Oxygen Reduction to Hydrogen Peroxide Catalyzed by Nickel Single-Atom Catalysts with Tetradentate N2 O2 Coordination in a Three-Phase Flow Cell, *Angew Chem Int Ed Engl,* **2020,** 59, 13057-13062.
21. Malko, D.; Lopes, T.; Symianakis, E.; Kucernak, A. R.,The Intriguing Poison Tolerance of Non-Precious Metal Oxygen Reduction Reaction (Orr) Catalysts, *Journal of Materials Chemistry A,* **2015,** 4, 142-152.
22. Akkurt, F.,Air Oxidation of Ferrous Iron in Water, *Journal of International Environmental Application and Science,* **2008,** 3, 409-414.
23. Ravel, B.; Newville, M.,Athena, Artemis, Hephaestus: Data Analysis for X-Ray Absorption Spectroscopy Using Ifeffit, *Journal of Synchrotron Radiation,* **2005,** 12, 537-537.
24. Wu, J.; Li, P.; Parra-Puerto, A.; Wu, S.; Lin, X.; Kramer, D.; Chen, S.; Kucernak, A.,Controllable Heteroatom Doping Effects of Cr Xco2-Xp Nanoparticles: A Robust Electrocatalyst for Overall Water Splitting in Alkaline Solutions, *ACS Applied Materials and Interfaces,* **2020,** 12, 47397-47407.
25. Tylus, U.; Jia, Q.; Strickland, K.; Ramaswamy, N.; Serov, A.; Atanassov, P.; Mukerjee, S.,Elucidating Oxygen Reduction Active Sites in Pyrolyzed Metal-Nitrogen Coordinated Non-Precious-Metal Electrocatalyst Systems, *Journal of Physical Chemistry C,* **2014,** 118, 8999-9008.
26. Larouche, N.; Stansfield, B. L.,Classifying Nanostructured Carbons Using Graphitic Indices Derived from Raman Spectra, *Carbon,* **2010,** 48, 620-629.
27. Kim, H. W.; Ross, M. B.; Kornienko, N.; Zhang, L.; Guo, J.; Yang, P.; McCloskey, B. D.,Efficient Hydrogen Peroxide Generation Using Reduced Graphene Oxide-Based Oxygen Reduction Electrocatalysts, *Nature Catalysis,* **2018,** 1, 282-290.
28. Ferrara, M.; Bevilacqua, M.; Melchionna, M.; Criado, A.; Crosera, M.; Tavagnacco, C.; Vizza, F.; Fornasiero, P.,Exploration of Cobalt@ N-Doped Carbon Nanocomposites toward Hydrogen Peroxide (H2o2) Electrosynthesis: A Two Level Investigation through the Rrde Analysis and a Polymer-Based Electrolyzer Implementation, *Electrochimica Acta,* **2020,** 364, 137287.
29. Chen, Y.; Jie, S.; Yang, C.; Liu, Z.,Active and Efficient Co-N/C Catalysts Derived from Cobalt Porphyrin for Selective Oxidation of Alkylaromatics, *Applied Surface Science,* **2017,** 419, 98-106.
30. Jung, E.; Shin, H.; Lee, B. H.; Efremov, V.; Lee, S.; Lee, H. S.; Kim, J.; Hooch Antink, W.; Park, S.; Lee, K. S.; Cho, S. P.; Yoo, J. S.; Sung, Y. E.; Hyeon, T.,Atomic-Level Tuning of Co-N-C Catalyst for High-Performance Electrochemical H2o2 Production, *Nat Mater,* **2020,** 19, 436-442.
31. Pan, F.; Zhang, H.; Liu, K.; Cullen, D.; More, K.; Wang, M.; Feng, Z.; Wang, G.; Wu, G.; Li, Y.,Unveiling Active Sites of Co2 Reduction on Nitrogen-Coordinated and Atomically Dispersed Iron and Cobalt Catalysts, *ACS Catalysis,* **2018,** 8, 3116-3122.
32. Wan, X.; Liu, X.; Li, Y.; Yu, R.; Zheng, L.; Yan, W.; Wang, H.; Xu, M.; Shui, J.,Fe–N–C Electrocatalyst with Dense Active Sites and Efficient Mass Transport for High-Performance Proton Exchange Membrane Fuel Cells, *Nature Catalysis,* **2019,** 2, 259-268.
33. S.R.Kelemen; G.N.George; M.L.Gorbaty,1. The X-Ray Photoelectron, *Fuel,* **1990,** 69, 939-944.
34. Wang, X. X.; Cullen, D. A.; Pan, Y. T.; Hwang, S.; Wang, M.; Feng, Z.; Wang, J.; Engelhard, M. H.; Zhang, H.; He,

Y.,Nitrogen-Coordinated Single Cobalt Atom Catalysts for Oxygen Reduction in Proton Exchange Membrane Fuel Cells, *Advanced Materials,* **2018,** 30, 1706758.
35. Shui, J.; Chen, C.; Grabstanowicz, L.; Zhao, D.; Liu, D. J.,Highly Efficient Nonprecious Metal Catalyst Prepared with Metal-Organic Framework in a Continuous Carbon Nanofibrous Network, *Proceedings of the National Academy of Sciences of the United States of America,* **2015,** 112, 10629-10634.
36. Jiang, K.; Back, S.; Akey, A. J.; Xia, C.; Hu, Y.; Liang, W.; Schaak, D.; Stavitski, E.; Nørskov, J. K.; Siahrostami, S.,Highly Selective Oxygen Reduction to Hydrogen Peroxide on Transition Metal Single Atom Coordination, *Nature communications,* **2019,** 10, 1-11.
37. Malko, D. Electrocatalytic and Catalytic Oxygen Reduction Utilising Transition Metal and Heteroatom Doped Carbon Materials. Ph.D. Dissertation, Imperial College London, 2016.
38. Bonakdarpour, A.; Lefevre, M.; Yang, R.; Jaouen, F.; Dahn, T.; Dodelet, J.-P.; Dahn, J.,Impact of Loading in Rrde Experiments on Fe–N–C Catalysts: Two-or Four-Electron Oxygen Reduction? , *Electrochemical and Solid State Letters,* **2008,** 11, B105.
39. Lee, S.; Kwak, D.-H.; Han, S.-B.; Hwang, E.-T.; Kim, M.-C.; Lee, J.-Y.; Lee, Y.-W.; Park, K.-W.,Synthesis of Hollow Carbon Nanostructures as a Non-Precious Catalyst for Oxygen Reduction Reaction, *Electrochimica Acta,* **2016,** 191, 805-812.
40. Bard, A. J.; Parsons, R.; Jordan, J., *Standard Potentials in Aqueous Solution*. CRC Press: 1985; p 852.
41. Shinagawa, T.; Garcia-Esparza, A. T.; Takanabe, K.,Insight on Tafel Slopes from a Microkinetic Analysis of Aqueous Electrocatalysis for Energy Conversion, *Scientific Reports,* **2015,** 5, 1-21.
42. Primbs, M.; Sun, Y.; Roy, A.; Malko, D.; Mehmood, A.; Sougrati, M. T.; Blanchard, P. Y.; Granozzi, G.; Kosmala, T.; Daniel, G.; Atanassov, P.; Sharman, J.; Durante, C.; Kucernak, A.; Jones, D.; Jaouen, F.; Strasser, P.,Establishing Reactivity Descriptors for Platinum Group Metal (Pgm)-Free Fe-N-C Catalysts for Pem Fuel Cells, *Energy and Environmental Science,* **2020,** 13, 2480-2500.
43. Pourbaix, M., *Atlas of Electrochemical Equilibria in Aqueous Solutions*. Pergamon Press: Oxford, 1966; p 644-644.
44. Figlarz, M.; Guenot, J.; Tournemolle, J. N.,Oxidation of Cobalt (Ii) Hydroxide to Oxide Hydroxide: Solids Evolution During Reaction, *Journal of Materials Science,* **1974,** 9, 772-776.

TOC figure